ChemPhysChem

Research Article
doi.org/10.1002/cphc.202400742

Chemistry Europe
European Chemical Societies Publishing

www.chemphyschem.org

Deciphering the Ce^{3+} to Ce^{4+} Evolution: Insight from X-ray Raman Scattering Spectroscopy at Ce $N_{4,5}$ Edges

Soumya K. Das,[a, b] Alessandro Longo,*[a, c] Eugenio Bianchi,[a, d] Claudio V. Bordenca,[e] Christoph J. Sahle,[a] Maria Pia Casaletto,[c] Alessandro Mirone,*[a] and Francesco Giannici[e]

Cerium oxide, or ceria, (CeO_2) is one of the most studied materials for its wide range of applications in heterogeneous catalysis and energy conversion technologies. The key feature of ceria is the remarkable oxygen storage capacity linked to the switch between Ce^{4+} and Ce^{3+} states, in turn creating oxygen vacancies. Changes in the electronic structure occur with oxygen removal from the lattice. Accordingly, the two valence electrons can be accommodated by the reduction of support cations where the electrons can be localized in empty *f* states of Ce^{4+} ions nearby due to small polaron hopping resulting in the formation of Ce^{3+}. Quantifying the different oxidation states in situ is crucial to understand and model the reaction mechanism.

Beside the different techniques that have been used to quantify Ce^{3+} and Ce^{4+} states, we discuss the use of X-ray Raman Scattering (XRS) spectroscopy as an alternative method. In particular, we show that XRS can observe the oxidation state changes of cerium directly in the bulk of the materials under realistic environmental conditions. The Hilbert++ code is used to simulate the XRS spectra and quantify accurately the Ce^{3+} and Ce^{4+} content. These results are compared to those obtained from in situ X-ray Diffraction (XRD) collected in parallel and the differences arising from the two different probes are discussed.

Introduction

Cerium(IV) oxide, or ceria, has been one of the most studied oxide materials in catalysis for decades, since it finds application as an active component in three-way catalysts, in catalytic material for the oxidation of CO, and hydrocarbons[1–3] and many other gas-solid reactions.[2]

In addition, combining ionic conductivity with catalytic properties, ceria finds applications in fuel cells and electrolyzers at intermediate to high temperatures.[2,4,5] The most important features in all these applications is the high density of oxygen vacancies, and the ability to incorporate and release molecular oxygen.[1,2] This property, defined as oxygen storage capacity (OSC), is connected to the reduction of Ce^{4+} to Ce^{3+}, acting as a reducing or oxidizing agent as a function of the reaction conditions.[1,2,6]

As an example, the high activity of metal nanoparticles supported on ceria in the oxidation of CO to CO_2 is explained by an enhanced vacancy formation process described with the Mars-van Krevelen mechanism.[1,6] In this mechanism, the surface oxygen atoms of ceria are involved in the oxidation reactions and are linked with oxygen lattice vacancy formation.[7–9]

In general, noble metals dispersed on the oxide surface facilitate the release of oxygen from ceria, further increasing its OSC at room temperature. In particular, in Au/ceria the oxidation and oxygen adsorption occur mainly in the peripheral sites at the metal-support interface.[10–13] These sites are the most active thanks to the presence of oxygen vacancies formed due to the Schottky junction established at the metal/support interface.[14] In all these examples, the formation of vacancies is deeply connected with the electronic change upon oxygen removal from the ceria support. When lattice oxygen ions (O^{2-}) are removed from the lattice and O_2 is evolved, the two valence electrons can be accommodated by the reduction of support cations.[12,13] In particular, the electrons can be localized in empty *f* states of Ce^{4+} ions nearby due to small polaron hopping resulting in the formation of Ce^{3+}.[15]

Remarkably, the capacity to adjust the redox couple and modify the Ce^{3+}/Ce^{4+} ratio transcends applications in heterogeneous catalysis and impacts also electrocatalyst and ceria based electrolytes used in SOFCs.[16,17] In fact, varying the amount of Ce^{3+} improves the oxygen evolution reaction (OER) perform-

[a] S. K. Das, A. Longo, E. Bianchi, C. J. Sahle, A. Mirone
European Synchrotron Radiation Facility, 71, Avenue des Martyrs, Grenoble F-38000, France
E-mail: alessandro.longo@esrf.fr
alessandro.mirone@esrf.fr

[b] S. K. Das
Laboratory for Chemical Technology, Ghent University, Technologiepark 125, 9052 Zwijnaarde, Belgium

[c] A. Longo, M. Pia Casaletto
Istituto per lo Studio dei Materiali Nanostrutturati (ISMN)-CNR, UOS Palermo, via Ugo La Malfa 153, Palermo 90146, Italy

[d] E. Bianchi
Politecnico di Milano, Piazza Leonardo da Vinci, 32, 20133 Milano MI, Italy

[e] C. V. Bordenca, F. Giannici
Dipartimento di Fisica e Chimica "Emilio Segrè", Università di Palermo, viale delle Scienze, I-90128 Palermo, Italy

Supporting information for this article is available on the WWW under https://doi.org/10.1002/cphc.202400742

ance of ceria-based hybrid catalysts. Increased levels of Ce^{3+} can activate ceria as an OER catalyst by enhancing ion conductivity and optimizing the binding energy of OH^- intermediates during the process.[16,18]

The redox properties of ceria have attracted the interest of the scientific community also for its potential use in biological systems, e.g. as a multi-antioxidant for sepsis treatment.[19] The two oxidation states of ceria nanoparticles, Ce^{3+} and Ce^{4+}, play a pivotal role in scavenging reactive oxygen species (ROS) and, in particular, Ce^{3+} is largely responsible for removing O^{2-} and $OH^{\cdot}$, associated with inflammatory response.[20] All these potentially innovative therapeutic tools are linked to the Ce^{4+}/Ce^{3+} switch, which can mimic the action of key antioxidant enzymes such as superoxide dismutase.[19,21–23]

An accurate control of the Ce^{4+}/Ce^{3+} ratio is necessary to tune the catalytic activity and biological response.[24] This is also connected to the formation of surface vacancies, which form in the nanoparticles. On the other end, the general understanding of vacancy formation is still a debated topic in catalysis,[25,26] since this is linked to the mechanistic aspect of the most oxidation reactions in which the ceria is involved. The electronic modifications in the lattice, the formation of Ce^{3+}, and the formation of oxygen vacancies are all intertwined during the oxidation and reduction reactions. For these reasons, the accurate quantification of the oxidation state in the lattice is probably the most important experimental parameter to assess in the study of ceria-based materials.

To this aim, many authors used X-ray absorption spectroscopy at the Ce L_3-edge, both employing conventional and high energy resolution fluorescence detection (HERFD).[27–30] In particular, Safonova et al. studied the electronic and the geometric structure of Ce^{3+} and Ce^{4+} in ceria nanoparticles under reducing conditions, showing that Ce^{3+} ions form both at the surface and in the near-surface layer.[27,30] However, since the L_3-edge mainly probes the *d* states rather than the *f* states, the mixing of the *f* and *d* states occurring in Ce^{3+} is difficult to be detected. Understanding the variation of the spectrum is, therefore, quite challenging since it is predominantly characterized by the Ce^{4+} features. Accordingly, the analysis of the spectra is not trivial and the study of the Ce^{3+} remains elusive. Thus, results are often not entirely conclusive and are controversially discussed and interpreted.[27–32]

Other authors measured the Ce $M_{4,5}$ edges using electron energy loss spectroscopy (EELS) in order to assess the presence of oxygen vacancies at the grain boundaries.[29,31] By analyzing quantitatively the M_4/M_5 ratio, they have revealed that oxygen non-stoichiometry plays a crucial role in the stable grain boundary structure of CeO_2. However, the measurements are quite surface sensitive and strongly affected by multiple scattering. The thickness of the samples and the limitation of the sample environment are important constraints, which render *in-situ* measurements very demanding.[29,31]

Gordon et al, by exploiting the *q* dependencies of the Ce $N_{4,5}$ edge via non-resonant inelastic X-ray scattering, or X-ray Raman Scattering (XRS), have revealed that the strong pre-threshold peaks, which are non-dipolar in character, are sensitive to *f*-occupation and dominate the spectrum at high *q*. The two different cations Ce^{3+} and Ce^{4+} show clear differences that can be studied and monitored upon the oxidation process.[33] The effectiveness of this spectroscopic tool for probing the physics and chemistry of *f*-electron systems, such as ceria, has been well-documented in previous studies.[9,34,35]

In the present work, we use XRS to examine the *in-situ* transformation of Ce^{3+} to Ce^{4+} during the oxidation process of cerium (III) sulfate hydrate in air. Cerium sulfate is a commonly used precursor in many wet-chemical syntheses of cerium oxide and it represents a well-defined model reaction for the more general Ce^{3+}/Ce^{4+} switch occurring in ceria systems. Our aim is to discuss both the strengths and drawbacks of this approach, taking into account data collected at different momentum transfer ranges. By applying this method, we can quantify the oxidation state changes of cerium ions in ceria directly and accurately, under realistic environmental conditions.

We use the Hilbert++ code to simulate the XRS spectra and quantify the Ce^{3+} and Ce^{4+} content. The results are compared and discussed with those obtained by in situ X-ray Diffraction (XRD) collected in parallel at ID20 before and after the oxidation treatment. Finally, this example shows how X-ray Raman Scattering (XRS) spectroscopy at the Ce $N_{4,5}$-edges can be an alternative approach to study the Ce^{3+} and Ce^{4+} transformation quantitatively. Advantages and drawbacks are also discussed. The method can be applied to others cations belonging to *f*-electron system, which have redox properties.

Methods and Experiments

Sample

In this work, we study the transformation of cerium sulfate hydrate[36] $Ce_2(SO_4)_3 \cdot 8H_2O$ (99.99%, Sigma-Aldrich), taken as a Ce^{3+} reference and a commonly used precursor in many wet-chemical syntheses of cerium oxide. CeO_2 (99.999%, NIST) was used as a Ce^{4+} reference. All samples were measured as pellets in a custom high-temperature oven provided by the ESRF sample environment group. The temperature in the cell was increased from 25 °C to 800 °C in air.

XRS and XRD Measurements

The XRS data were measured on beamline ID20 of the ESRF, using radiation from three U26 undulators that was monochromatized by a high heat-load Si(111) double crystal monochromator and a successive Si(311) channel-cut post-monochromator. The monochromatic X-ray beam was focused to approximately 50×50 μm^2 (V×H) using a Kirkpatrick-Baez mirror. We used the large solid angle spectrometer of ID20[37] to record the XRS signals. Spectra were collected at four median scattering angles (40°, 80°, 121°, 135°) for a total of 48 spherically bent Si(660) analyzer crystals, corresponding to momentum transfers *q* of 3.4±0.2 (low q), 6.3±0.2 (med q), 8.9±0.2 and 9.6±0.2 (high q) $Å^{-1}$, respectively. In order to create losses in the vicinity of the cerium $N_{4,5}$ edges, we scanned the incident energy from 9.787 to 9.887 *keV* (100 *eV* loss across the $N_{4,5}$ Ce edge at 109 *eV*) at a constant analyzer energy of 9.7 *keV*. The overall energy resolution was 0.7 *eV* (FWHM). As the difference in *q* between the two highest scattering angles is small, the data set acquired at the higher *q* were averaged, to provide the high *q* XRS spectra. All data were processed using the XRStools software

package.[38] All the sets of data were normalized over a range of 100–150 *eV* energy loss, corresponding to the cerium edge. The XRD patterns were acquired in parallel under in situ condition with the XRS measurements at an incident energy of 9.92 *keV* (corresponding to a wavelength of 1.25 Å). The XRD data were processed using the pyFAI software[39] after calibration on a CeO_2 sample used as a reference. The Rietveld refinements of the XRD patterns were obtained using the GSAS-II software.[40] A schematic elaborating the experimental plan is presented in Figure 1.

Hilbert++ and ab-Initio Spectra Simulations

All multiplet calculations discussed in this work, which are essential for deriving the Ce^{3+}/Ce^{4+} ratio presented below, were conducted using the Hilbert++ code.[41] This software facilitated the analysis of spectroscopic data and enabled the determination of oxidation state ratios based on the measured spectra.[41,42] The spectra have been calculated for the Ce^{4+} and Ce^{3+} ions, using a ligand field as obtained by projection of selected ligand orbitals onto well localized Wannier orbitals. We used Quantum Espresso[43,44] to determine the self-consistent electronic ground state of CeO_4 and produced projections of the 2*p* orbitals of ligand oxygen atoms using the Wannier90 code.[45,46] The analysis of the Wannier Hamiltonian shows a crystal field of the order of one tenth of *eV* for the 4*f* shell. This weak perturbation has a negligible effect on the calculated spectra and we will see that, beside the giant-dipole resonance which we will model as a unbound state, the spectra is shaped by merely intra-atomic interactions.

The Hilbert++ code computes spherically averaged X-ray Raman spectra for a given magnitude of momentum transfer *q*. For low values of *q*, characterized by $2\pi/q$ being smaller than the inverse of the average radius of the 4*d* orbital, the multipole expansion of the Thomson scattering term for the $N_{4,5}$ transitions is predominantly influenced by the dipolar term. The amplitude of the subsequent term in the expansion is approximately proportional to the amplitude of the dipole term times qr_{4d}^2. Specifically, for the dipolar term the final hole-electron pair can have, by selection rules, only $L=1$ angular momentum and it turns out that such state is energetically shifted upwards due to the core-hole entanglement which results in an enhanced Coulomb term equal to twice the Slater integral G_1 between the 4*d* and 4*f* orbitals. This Coulomb term plays a significant role in determining the energy positioning of the $L=1$ peak within the spectra.[47] The transitions to $L=3$ and $L=5$ states become visible at higher *q*, and, for these transitions, the core-hole exchange contribution is much weaker, and resulting peaks are found at lower energies.[35]

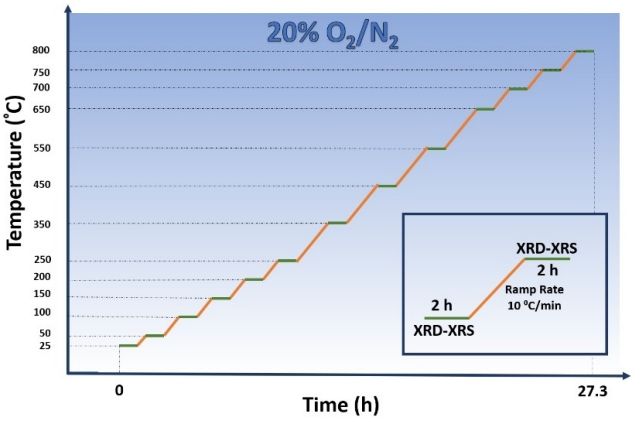

Figure 1. A schematic of experimental plan for in-situ XRD-XRS is presented. Inset explains that the XRD-XRS measurements were performed under 20% O_2/N_2 for 2 h, at each step after rising the temperature (with a ramp rate of 10 °C/min). The experiment took 27.3 h to finish.

In order to assess the effect of the entanglement-driven 4*f* photoelectron shift toward high energy on the spectra, and also its possible 4*f* photoelectron core-hole exchange-induced delocalization and peak broadening, we have performed a calculation with a modified version of the Xspectra code from the Quantum Espresso suite, which unifies Hilbert++ and Lanczos treatment of the photo-electron propagator. In such an approach, initially, a self-consistent calculation is conducted for a CeO_2 supercell, wherein a Ce site is intentionally charged with a hole in the 4*d* shell. Following this, within the resultant self-consistent field (SCF) potential, the propagator is computed not only for the photo-electron's one-particle wavefunction but also for the direct product of the core-hole wavefunction and the photo-electron wavefunction. This approach allows for a comprehensive assessment of the electronic structure and interactions within the charged Ce site in the CeO_2 lattice. Finally, the giant dipole resonance spectra have been obtained with a prototype version of Xspectruplet code (see SI) where the entanglement between the photo-electron and the core-hole is considered.

Results and Discussion

Figure 2 summarizes the thermal decomposition of the cerium sulfate sample in air from two complementary points of view: crystal structure and electronic structure. As reported in the literature,[36] the material dehydrates first and then undergoes a series of phase transitions and chemical transformations when subjected to temperatures ranging from 25 °C and 800 °C. The results of Rietveld analyses of the XRD patterns (shown in full in Figure S1) are reported in Tables 1 and 2. The identified crystallographic phases align well with previous studies.[36]

The full quantitative analysis of the XRD patterns collected at 350 °C, to 750 °C proved more challenging, due to the incomplete identification of the crystal phases. Therefore, the results at these temperatures should be considered as qualitative. The initial decomposition temperature of $Ce_2(SO_4)_3$ aligns well with the values previously reported in the literature.[36] As reported in Figure 2 A (gray box), cerium oxide starts appearing at 650 °C and subsequently undergoes grain growth and increased crystallinity as evidenced by the sharper peaks at higher temperatures Consistent with previous research, the formation of pure cerium oxide is completed at around $T=$ 800 °C.[36] Figure 2 B reports the Ce $N_{4,5}$ edge XRS spectra at both low and high *q* in the same temperature range. As we showed in a previous study, the non-dipole multiplet structures are very sensitive to the redox treatment, especially at high *q* where the contribution of the giant dipole resonance is low.[9] The XRS spectra at the $N_{4,5}$ edges at high *q* are dominated by the pre-threshold peaks of the Ce 4*f* multiplet. These peaks correspond to different contributions from various transition orders, including the 1st-order (dipole), 3rd-order (octupole), and 5th-order (triakontadipole) transitions.[33]

During the transformation from Ce^{3+} to Ce^{4+}, the exact distribution of transitions for the different cation changes, and this allows for an unambiguous assignment of the oxidation

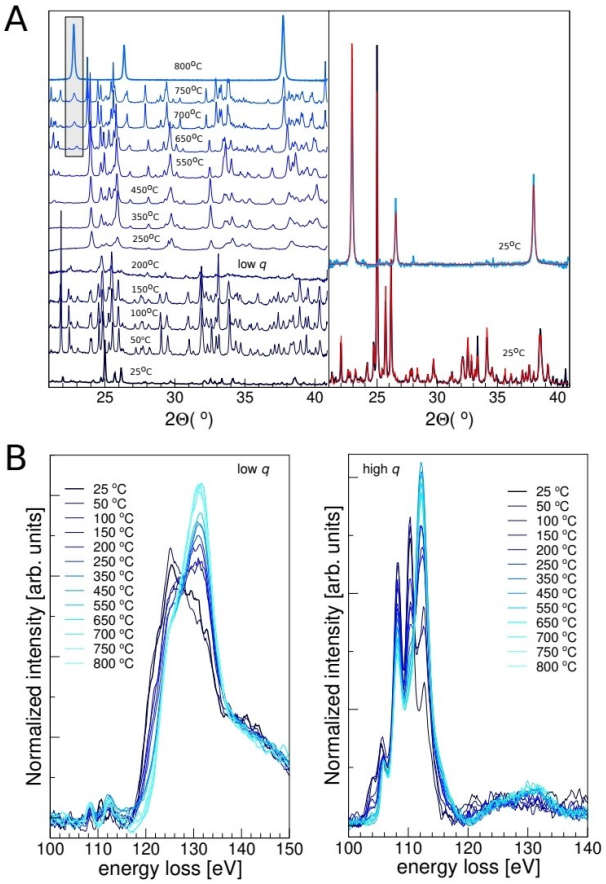

Figure 2. Panel A – right: experimental XRD patterns from 25 °C to 800 °C; left: Rietveld refinements of XRD at 25 °C, before (dark blue) and after (blue) the thermal treatment. Panel B: Ce $N_{4,5}$ edge XRS spectra at low q (left) and high q (right) from 25 °C to 800 °C.

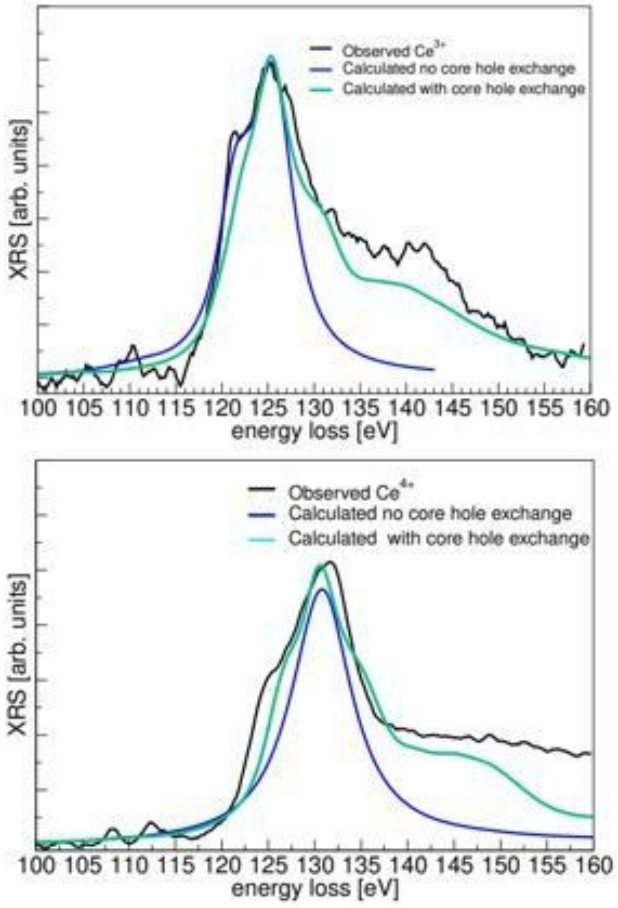

Figure 3. Panel A: Observed Ce^{3+} and Quantum Espresso calculation of the Ce $N_{4,5}$ edge using the Xspectruplet code. The Blue line shows the calculated spectrum without core-hole exchange, the green-turquoise line shows the spectrum which takes into account the core-hole exchange and entanglement. Panel B: Observed Ce^{4+} and Quantum Espresso calculation of the Ce $N_{4,5}$ edge using the Xspectruplet code. The Blue line shows the calculated spectrum without core-hole exchange, the green-turquoise line shows the spectrum which takes into account the core-hole exchange and entanglement.

state. In the following, we first consider the evolution of the spectra at a low momentum transfer ($q = 3.5$ Å^{-1}). The spectrum at 25 °C at low q exhibits, as expected, the Ce^{3+} features.[33] Upon thermal treatment, the transformation to Ce^{4+} is testified by the continuous shift of the edge towards higher energy and changes in the overall spectral shape, resembling that of reference ceria (see Figure 2B).[9,33] The spectrum at $T = 200$ °C at low q already exhibits a non-negligible contribution from Ce^{4+} (specifically, the octupole component), which becomes predominant already at $T = 350$ °C.[33] According to the calculations discussed in the previous section, the shoulder observed at 125 eV energy loss, which might be incorrectly attributed to a Ce^{3+} component, is rather related, to some extent, to the interactions with the continuum. The results of these calculations are reported in Figure 3 for both Ce^{3+} and Ce^{4+} cations respectively. Disentangling this contribution is complex and not always straightforward. As evident in Figure 3 the core hole exchange impact significantly the spectrum at the low q, so the interpretation of the Ce $N_{4,5}$ edge is challenging and would require more complex calculations to disentangle the different contributions in the spectrum. Thus, analyzing the Ce $N_{4,5}$ edge at low q tends towards a qualitative rather than quantitative approach.

More detailed and conclusive XRS data are obtained at high q ($q = 9.5$ Å^{-1}) (refer to Figure 2B, high q). In this scenario, the interaction with the continuum does not significantly impact the pre-edge multiplets as it occurs at higher energy. Upon examining Figure 2 B (right column), it is evident that at high q even at 25 °C, the Ce $N_{4,5}$ edge spectrum exhibits characteristics typical of Ce^{3+}. Five sharp peaks corresponding to non-dipole atomic-like transition $4d^{10}-4f^{n} \rightarrow 4d^{9}4f^{n+1}$ of different symmetry can be assigned at different energy values, corresponding approximately to 104, 108, 110 and 114 *eV* respectively.[33] The different peaks correspond to the position of the different transition orders.[33]

In the case of Ce^{4+} only three sharp peaks can be detected at approximately 104, 108, and 112 *eV* energy loss, respectively. Thus, the transformation between Ce^{3+} to Ce^{4+} through the

Table 1. Crystalline phases and their weight fraction from Rietveld refinement of the XRD, as a function of temperature. Uncertainty is approximately 1%.

T (°C)	Compound Name	Chemical Formula	Phase %
25	Dicerium (III) trisulfate tetrahydrate	$Ce_2(SO_4)_3 \cdot 4H_2O$	100
50	Dicerium (III) trisulfate tetrahydrate	$Ce_2(SO_4)_3 \cdot 4H_2O$	100
100	Dicerium (III) trisulfate tetrahydrate	$Ce_2(SO_4)_3 \cdot 4H_2O$	100
150	Dicerium (III) trisulfate tetrahydrate Oxonium cerium (III)sulfate hydrate	$Ce_2(SO_4)_3 \cdot 4H_2O$ $[H_3O][Ce(SO_4)_2] \cdot H_2O$	67 33
250	Dicerium (III) trisulfate tetrahydrate Cerium (III) hemioxonium sesquisulfate hemihydrogensulfate	$Ce_2(SO_4)_3 \cdot 4H_2O$ $Ce(H_3O)_{0.5}(SO_4)_{1.5}(HSO_4)_{0.5}$	78 22
350	Dicerium (III) trisulfate tetrahydrate Cerium (IV) oxide sulfate hydrate	$Ce_2(SO_4)_3 \cdot 4H_2O$ $CeO(SO_4) \cdot H_2O$	70 30
450	Dicerium (III)trisulfate tetrahydrate Cerium (IV) oxide sulfate hydrate Cerium hydroxide sulfate	$Ce_2(SO_4)_3 \cdot 4H_2O$ $CeO(SO_4) \cdot H_2O$ $Ce(OH)(SO_4)$	68 14 17
550	Dicerium (III) trisulfate tetrahydrate Cerium (IV) oxide sulfate hydrate	$Ce_2(SO_4)_3 \cdot 4H_2O$ $CeO(SO_4) \cdot H_2O$	71 29
650	Cerium carbonate Cerium (IV) oxide Cerium (III) oxide	$[Ce(H_2O)]_2(C_2O_4)_2(CO_3) \cdot (H_2O)_{2.5}$ CeO_2 Ce_2O_3	98 1.1 0.9
700	Cerium carbonate Cerium (IV) oxide Cerium (III) oxide	$[Ce(H_2O)]_2(C_2O_4)_2(CO_3) \cdot (H_2O)_{2.5}$ CeO_2 Ce_2O_3	93 44 2.6
750	Cerium carbonate Cerium (IV) oxide	$[Ce(H_2O)]_2(C_2O_4)_2(CO_3) \cdot (H_2O)_{2.5}$ CeO_2	90.6 9.4
800	Cerium (IV) oxide	CeO_2	100

Table 2. Results of Rietveld refinements of the XRD patterns, a, b, and c are reported in Å, and the angles in (°) for the non-orthogonal space groups. Uncertainty is on the last digit.

T (°C)	Compound Name	Space Group	a	b	c	$\alpha\beta\gamma$
25	$Ce_2(SO_4)_3 \cdot 4H_2O$	$P2_1/n$	13.13	7.255	11.39	90. 133.13 90.
50	$Ce_2(SO_4)_3 \cdot 4H_2O$	$P2_1/n$	13.10	7,220	13.58	90. 133.11 90.
100	$Ce_2(SO_4)_3 \cdot 4H_2O$	$P2_1/n$	13.17	7.266	13.45	90. 133.12 90.
150	$Ce_2(SO_4)_3 \cdot 4H_2O$ $[H_3O][Ce(SO_4)_2] \cdot H_2O$	$P2_1/n$ $P2_1/n$	13.17 9.351	7.285 9.923	13.30 8.450	90. 133.13 90. 90. 133.14 90.
250	$Ce_2(SO_4)_3 \cdot 4H_2O$ $Ce(H_3O)_{0.5}(SO_4)_{1.5}(HSO_4)_{0.5}$	$P2_1/n$ P m	13.20 7.091	7.256 5.409	13.38 9.171	90. 133.11 90. 90. 95.30 90.
350	$Ce_2(SO_4)_3 \cdot 4H_2O$ $CeO(SO_4) \cdot H_2O$	$P2_1/n$ $P\ 2_1\ 2_1\ 2_1$	13.13 11.99	7.251 8.243	13.36 4.321	90. 133.10 90.
450	$Ce_2(SO_4)_3 \cdot 4H_2O$ $CeO(SO_4) \cdot H_2O$ $Ce(OH)(SO_4)$	$P2_1/n$ $P\ 2_1\ 2_1\ 2_1$ $P2_1/c$	13.14 11.99 4.511	7.251 8.277 12.56	13.36 4.328 7.131	90. 133.12 90. 90. 133.12 90.
550	$Ce_2(SO_4)_3 \cdot 4H_2O$ $CeO(SO_4) \cdot H_2O$	$P2_1/n$ $P\ 2_1\ 2_1\ 2_1$	13.21 11.98	7.253 8.268	13.37 4.329	90. 133.11 90.
650	$[Ce(H_2O)]_2(C_2O_4)_2(CO_3) \cdot (H_2O)_{2.5}$ CeO_2 Ce_2O_3	P-1 Fm-3m P-3m 1	6.329 5.435 3.861	8.748 5.435 3.861	12.97 5.435 6.071	105. 90. 105. 90 90 120
700	$[Ce(H_2O)]_2(C_2O_4)_2(CO_3) \cdot (H_2O)_{2.5}$ CeO_2 Ce_2O_3	P-1 Fm-3m P-3m 1	6.293 5.488 3.891	8.768 5.488 3.891	12.94 5.488 6.073	105. 90. 105. 90. 90. 120.
750	$[Ce(H_2O)]_2(C_2O_4)_2(CO_3) \cdot (H_2O)_{2.5}$ CeO_2	P-1 Fm-3m	6.307 5.491	8.768 5.491	12.98 5.491	105. 90. 105.
800	CeO_2	Fm-3m	5.491	4.491	5.491	

evolution of these peaks can be followed unambiguously. As shown in Figure 2B, the XRS spectra begin to change already at 50 °C. At this temperature, we first observe a decrease in the peak at 112 *eV*. It is only after reaching $T = 100$ °C that the

amount of Ce^{4+} begins to increase. Indeed, at 150–200 °C, the peak at 114 eV starts to rise, indicating the formation of Ce^{4+}. By $T = 350$ °C this component is predominant in the spectrum. By comparing the two different q at the specific spectral features we can conclude that: (i) at low q it is significant the edge shifts from 118 to 121–122 *eV* energy loss; (ii) at high q, notable modifications occur in the peaks at 102, 104, 108, and 112 *eV*, respectively. Specifically, the low-energy feature at 102 *eV* energy loss disappears and the intensity ratio of the peaks at 104, 108, and 112 *eV* changes, eventually making the peak at 114 *eV* predominant.

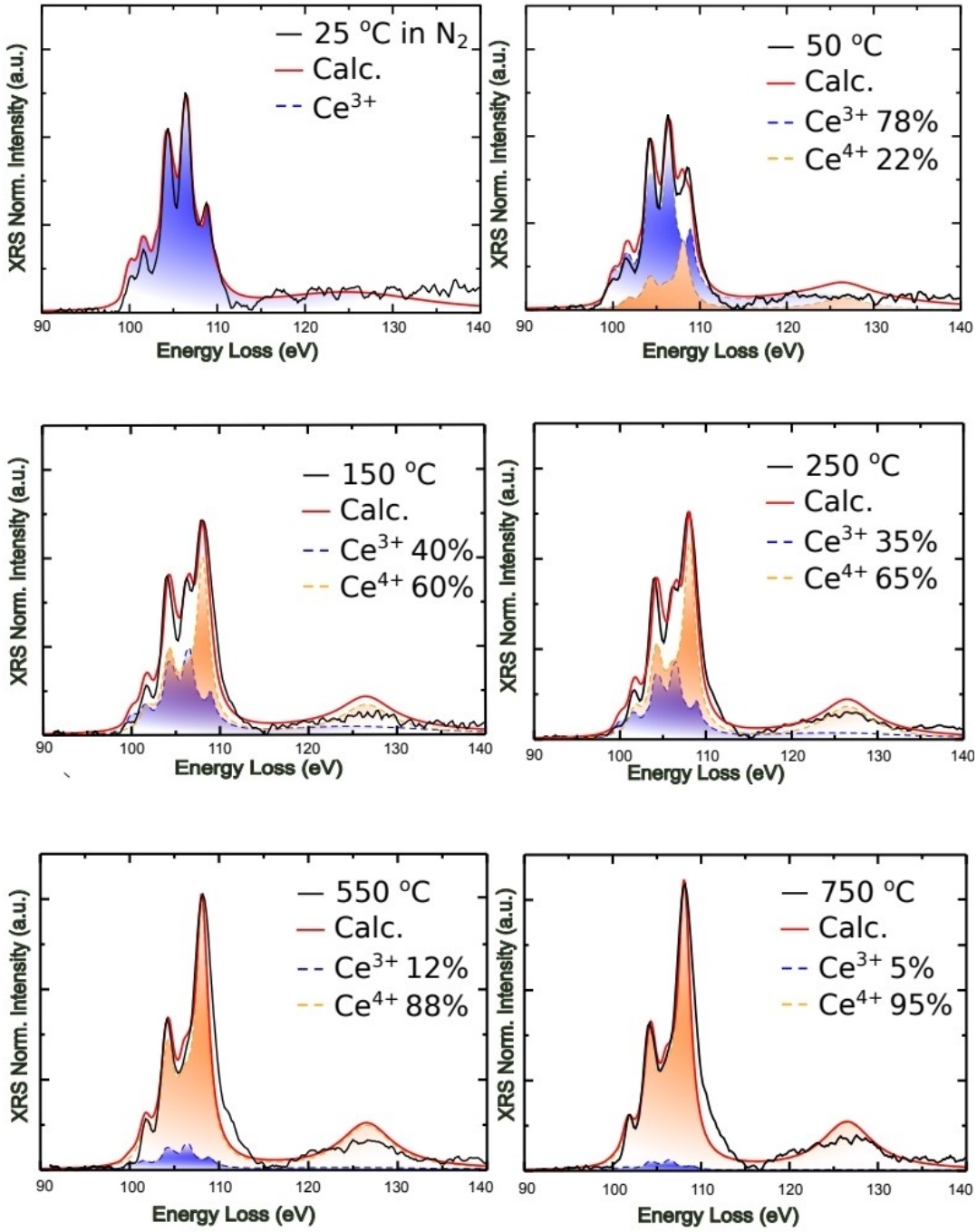

Figure 4. Linear combination fitting of the spectrum obtained in temperature range 25–750 °C showing the contribution of Ce^{3+} and Ce^{4+}.

According to the XRD results reported in Tables 1 and 2, the formation of Ce^{4+}, primarily associated with the formation of cerium oxide, is observed around 550 °C. This finding agrees with previous literature that identified a mixture of Ce^{3+} and Ce^{4+} at the same temperature reported here.[36] The apparent disagreement with the XRS, which indicates the formation of Ce^{4+} at a lower temperature (50 °C), is not surprising. Indeed, the XRD is sensitive to the long-range order, so XRD detects the Ce^{4+} only when some ceria or Ce^{3+}-doped ceria crystallites are formed. On the other hand, XRS, probing both the bulk and surface of the sample, reveals the presence of Ce^{4+} also during an incipient crystallization and in non-crystalline regions during a chemical transformation. It is important to note that the detection limit of the technique for Ce^{4+} under these experimental conditions is less than 5–10%. Interestingly, compared to other studies focusing on assessing the formation of Ce^{3+} using Ce $L_{2,3}$ edges,[30] the spectral features reported here particularly, at high q are well-defined and can be readily monitored and evaluated during thermal treatment in air under *in-situ* conditions. Additionally, unlike the $M_{4,5}$ edges,[31] the Ce $N_{4,5}$ edges can be measured without the need for a vacuum environment, allowing for bulk material probing.[9]

Based on these observations it can be assessed that the $N_{4,5}$ edges can be a valid alternative method to investigate the Ce^{3+}/Ce^{4+} ratio in cerium-based materials. Motivated by this conclusion for a methodological purpose, we have investigated quantitatively the formation of cerium oxide obtained from cerium sulfate by doing a thermal treatment in air. For the motivation discussed so far concerning the interaction with the continuum, we have limited the analysis on the XRS data collected at high q. For the linear combination fitting, each calculated spectrum is convoluted with a Fano line shape to account for the interaction with the continuum (see Figure S2). This convolution mainly dampens out the dipole contribution, which would be too strong in the calculated signals.[9]

Following the approach of previous theoretical studies, Ce $N_{4,5}$ edge spectra at different q have been simulated within the Hilbert++ scheme (see Figure S2). In this case, since it is not relevant at these energy values, interactions between the crystal-field-split final state multiplets with the continuum have been disregarded.[41,42] A full description of the underlying theory and its numerical procedure is reported elsewhere.[9,41,42] The method allows for the consideration of the q-dependence of *d-d* and *d-f* excitations and the evaluation of pre-threshold resonances outside the dipole limit.[42] To analyze the XRS spectra, two ionic configurations, Ce^{3+} (initial state $4d^{10}4f^{1}$) and Ce^{4+} ($4d^{10}4f^{0}$), were adopted. To simulate the spectrum of cerium oxide, Ce^{4+} was surrounded by eight oxygen atoms according to the Fm-3m crystallographic arrangement of CeO_2. On the other hand, for the spectrum of Ce^{3+}, only seven oxygens were placed around the trivalent cation, assuming the P-3m1 space group arrangement of Ce_2O_3. For consistency, the energy position and shape of both Ce^{3+} and Ce^{4+} components were fixed at the values obtained from the analysis of the references reported in Figure 4.

The linear combination fitting of the spectra using theoretical components is shown in Figure 4 for selected temperatures (see SI). The complete evolution of the Ce^{3+} and Ce^{4+} fractions during the thermal treatment is reported in Figure 5, giving a comprehensive and quantitative picture of the chemical transformations in situ. We detect a rather fast initial oxidation of Ce^{3+}, followed by a slower continuous process that is likely limited by the gas diffusion inside the pellet sample until approximately 800 °C.[48] The importance of such an approach transcends this particular case, and is readily generalized to any chemically important system (catalysts, solid electrolyte) where the cerium redox couple plays an important role. The peculiarities of photoelectron spectroscopy or soft X-ray spectroscopy (which are limited to the surface) or diffraction (limited to crystalline domains) are therefore complemented in this alternative quantitative approach.

Conclusions

In this study, the evolution of X-ray Raman scattering (XRS) spectra collected at the Ce $N_{4,5}$ edges is followed in situ, both at low and high q, to monitor the thermal decomposition of cerium (III) sulfate to cerium (IV) oxide in air. We show that the data collected at low q are influenced by the interaction with the continuum so that a quantitative determination of cerium cation ratios is challenging. On the other hand, spectra at high q values are unaffected by these constraints, and allow an accurate quantitative monitoring of the chemical transformation, since the relative concentrations of Ce^{3+} and Ce^{4+} determine the fine features of the XRS spectra at high q. All spectra were simulated using the Hilbert++ scheme, where theoretical signals are combined through linear combination analysis to achieve the best agreement with the experiment. Our results demonstrate that after a faster onset, the formation of cerium (IV) oxide proceeds slowly and continuously being limited by the oxygen gas diffusion in the pellet, until approximately 800 °C. We conclude that the $N_{4,5}$ absorption edges as probed by XRS are promising and unique tools to investigate the chemistry of *f*-electron systems that involve redox behavior.

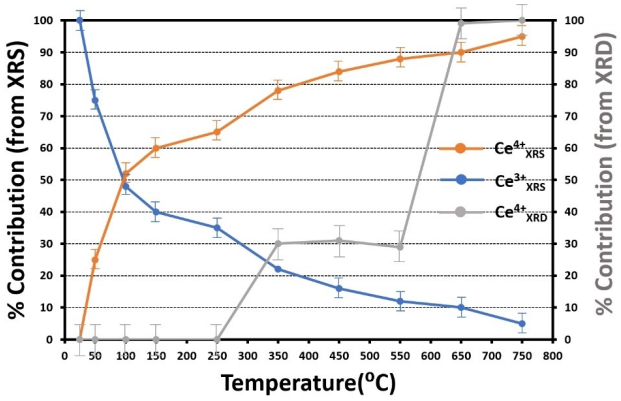

Figure 5. Amount of Ce^{4+} (orange) and Ce^{3+} (blue) obtained from XRS spectra and Ce^{4+} (grey) obtained from XRD spectra as a function of temperature.

We expect that by increasing the size of the Hilbert space the agreement with the experimental spectra will improve further, especially for the Ce^{3+} ion for which the entanglement with the 4*f* spectator electron should not be neglected. Further developments of the code will extend Xspectruplet to the Resonant Inelastic X-ray Scattering (RIXS) case, allowing to calculate the whole spectra of multipolar contributions from low to high *q*.

Acknowledgements

The authors thank the support of the European Synchrotron Radiation Facility (ESRF) Grenoble, France for in house beamtime IHCH1633 and IHCH1634. Florent Gerbon (ID20 staff) is kindly acknowledged for the his during the measurements. F.G. acknowledges partial financial support by the European Union – Next Generation EU (componente M4 C2, investimento 1.1) through grant PRIN 2022 PNRR P20224RBBX CUP B53D2302745 0001.

Conflict of Interests

The authors declare no conflict of interest.

Data Availability Statement

The data that support the findings of this study are available from the corresponding author upon reasonable request.

Keywords: X-ray Raman Scattering Spectroscopy · Ce N45 edges · Hilbert + + · XRD · Oxidation

[1] A. Trovarelli, *Catalysis by Ceria and Related Materials*, World Scientific **2002**.
[2] A. Trovarelli, *Catal. Rev.* **1996**, *38*, 439–520.
[3] T. Bunluesin, R. J. Gorte, G. W. Graham, *Appl. Catal. B* **1998**, *15*, 107–114.
[4] A. F. Diwell, R. R. Rajaram, H. A. Shaw, T. J. Truex, in *Stud. Surf. Sci. Catal.*, Elsevier **1991**, 139–152.
[5] M. Haruta, T. Kobayashi, H. Sano, N. Yamada, *Chem. Lett.* **1987**, *16*, 405–408.
[6] P. Mars, D. W. Van Krevelen, *Chem. Eng. Sci.* **1954**, *3*, 41–59.
[7] F. Esch, S. Fabris, L. Zhou, T. Montini, C. Africh, P. Fornasiero, G. Comelli, R. Rosei, *Science* **2005**, *309*, 752–755.
[8] C. T. Campbell, C. H. F. Peden, *Science* **2005**, *309*, 713–714.
[9] A. Longo, A. Mirone, E. D. C. Gallerande, C. J. Sahle, M. P. Casaletto, L. Amidani, S. A. Theofanidis, F. Giannici, *Cell Reports Phys. Sci.* **2023**, *4*.
[10] Y.-G. Wang, D. Mei, V.-A. Glezakou, J. Li, R. Rousseau, *Nat. Commun.* **2015**, *6*, 6511.
[11] L.-W. Guo, P.-P. Du, X.-P. Fu, C. Ma, J. Zeng, R. Si, Y.-Y. Huang, C.-J. Jia, Y.-W. Zhang, C.-H. Yan, *Nat. Commun.* **2016**, *7*, 13481.
[12] Y. Li, S. Li, M. B, ä, umer, E. A. Ivanova-Shor, L. V. Moskaleva, *ACS Catal.* **2020**, *10*, 3164–3174.
[13] M. Lohrenscheit, C. Hess, *ChemCatChem* **2016**, *8*, 523–526.
[14] J. C. Frost, *Nature* **1988**, *334*, 577–580.
[15] J. J. Plata, A. M. M, á, rquez, J. F. Sanz, *J. Phys. Chem. C* **2013**, *117*, 14502–14509.
[16] Z. A. Feng, F. El Gabaly, X. Ye, Z.-X. Shen, W. C. Chueh, *Nat. Commun.* **2014**, *5*, 4374.
[17] F. Giannici, G. Gregori, C. Aliotta, A. Longo, J. Maier, A. Martorana, *Chem. Mater.* **2014**, *26*, 5994–6006.
[18] J. Yu, Z. Wang, J. Wang, W. Zhong, M. Ju, R. Cai, C. Qiu, X. Long, S. Yang, *ChemSusChem* **2020**, *13*, 5273–5279.
[19] C. Korsvik, S. Patil, S. Seal, W. T. Self, *Chem. Commun.* **2007**, *35*, 1056–1058.
[20] M. Soh, D. Kang, H. Jeong, D. Kim, D. Y. Kim, W. Yang, C. Song, S. Baik, I. Choi, S. Ki, *Angew. Chem.* **2017**, *129*, 11557–11561.
[21] I. Celardo, M. De Nicola, C. Mandoli, J. Z. Pedersen, E. Traversa, L. Ghibelli, *ACS Nano* **2011**, *5*, 4537–4549.
[22] A. M. Mathew, P. V. Sreya, K. Venkatesan, A. Ganesan, D. K. Pattanayak, *ACS Appl. Bio Mater.* **2023**, *6*, 2284–2294.
[23] Y. G. Kim, Y. Lee, N. Lee, M. Soh, D. Kim, T. Hyeon, *Adv. Mater.* **2024**, *36*, 2210819.
[24] A. Gupta, S. Das, C. J. Neal, S. Seal, *J. Mater. Chem. B* **2016**, *4*, 3195–3202.
[25] A. Longo, F. Giannici, M. P. Casaletto, M. Rovezzi, C. J. Sahle, P. Glatzel, Y. Joly, A. Martorana, *ACS Catal.* **2022**, *12*, 3615–3627.
[26] M. Ziemba, C. Schilling, M. V. Ganduglia-Pirovano, C. Hess, *Acc. Chem. Res.* **2021**, *54*, 2884–2893.
[27] R. Kopelent, J. A. van Bokhoven, J. Szlachetko, J. Edebeli, C. Paun, M. Nachtegaal, O. V. Safonova, *Angew. Chem.* **2015**, *127*, 8852–8855.
[28] J. Bansmann, A. M. Abdel-Mageed, S. Chen, C. Fauth, T. Häring, G. Kučerová, Y. Wang, R. J. Behm, *Catalysts* **2019**, *9*, 785.
[29] Y. Zhang, S. Zhao, J. Feng, S. Song, W. Shi, D. Wang, H. Zhang, *Chem* **2021**, *7*, 2022–2059.
[30] O. V. Safonova, A. A. Guda, C. Paun, N. Smolentsev, P. M. Abdala, G. Smolentsev, M. Nachtegaal, J. Szlachetko, M. A. Soldatov, A. V. Soldatov, *J. Phys. Chem. C* **2014**, *118*, 1974–1982.
[31] K. Song, H. Schmid, V. Srot, E. Gilardi, G. Gregori, K. Du, J. Maier, P. A. van Aken, *Apl Mater.* **2014**, *2*, 3.
[32] L. Palys, D. Stephen, Z. Mao, S. T. Mergelsberg, D. Boglaienko, Y. Chen, L. Liu, Y. Bae, B. Jin, J. A. Sommers, *Langmuir* **2024**, *40*, 4350–4360.
[33] R. A. Gordon, G. T. Seidler, T. T. Fister, M. W. Haverkort, G. A. Sawatzky, A. Tanaka, T. K. Sham, *Europhys. Lett.* **2007**, *81*, 26004.
[34] M. Sundermann, H. Yavaş, K. Chen, D. J. Kim, Z. Fisk, D. Kasinathan, M. W. Haverkort, P. Thalmeier, A. Severing, L. H. Tjeng, *Phys. Rev. Lett.* **2018**, *120*, 16402.
[35] S. Sen Gupta, J. A. Bradley, M. W. Haverkort, G. T. Seidler, A. Tanaka, G. A. Sawatzky, *Phys. Rev. B: Condens. Matter Mater. Phys.* **2011**, *84*, 75134.
[36] J. A. Poston, Jr, R. V. Siriwardane, E. P. Fisher, A. L. Miltz, *Appl. Surf. Sci.* **2003**, *214*, 83–102.
[37] S. Huotari, C. J. Sahle, C. Henriquet, A. Al-Zein, K. Martel, L. Simonelli, R. Verbeni, H. Gonzalez, M.-C. Lagier, C. Ponchut, *J. Synchrotron Radiat.* **2017**, *24*, 521–530.
[38] C. J. Sahle, A. Mirone, J. Niskanen, J. Inkinen, M. Krisch, S. Huotari, *J. Synchrotron Radiat.* **2015**, *22*, 400–409.
[39] E. B. Knudsen, H. O. Sørensen, J. P. Wright, G. Goret, J. Kieffer, *J. Appl. Crystallogr.* **2013**, *46*, 537–539.
[40] B. H. Toby, R. B. Von Dreele, *J. Appl. Crystallogr.* **2013**, *46*, 544–549.
[41] A. Mirone, M. Sacchi, S. Gota, *Phys. Rev. B* **2000**, *61*, 13540.
[42] A. Longo, R. Wernert, A. Iadecola, C. J. Sahle, L. Stievano, L. Croguennec, D. Carlier, A. Mirone, *J. Phys. Chem. C* **2022**, *126*, 19782–19791.
[43] P. Giannozzi, S. Baroni, N. Bonini, M. Calandra, R. Car, C. Cavazzoni, D. Ceresoli, G. L. Chiarotti, M. Cococcioni, I. Dabo, *J. Phys. Condens. Matter* **2009**, *21*, 395502.
[44] P. Giannozzi, O. Andreussi, T. Brumme, O. Bunau, M. B. Nardelli, M. Calandra, R. Car, C. Cavazzoni, D. Ceresoli, M. Cococcioni, *J. Phys. Condens. Matter* **2017**, *29*, 465901.
[45] A. A. Mostofi, J. R. Yates, Y.-S. Lee, I. Souza, D. Vanderbilt, N. Marzari, *Comput. Phys. Commun.* **2008**, *178*, 685–699.
[46] A. A. Mostofi, J. R. Yates, G. Pizzi, Y.-S. Lee, I. Souza, D. Vanderbilt, N. Marzari, *Comput. Phys. Commun.* **2014**, *185*, 2309–2310.
[47] G. Van Der Laan, *Phys. Rev. B: Condens. Matter Mater. Phys.* **2012**, *86*, 35138.
[48] G. Deganello, F. Giannici, A. Martorana, G. Pantaleo, A. Prestianni, A. Balerna, L. F. Liotta, A. Longo, *J. Phys. Chem. B* **2006**, *110*, 8731–8739.

Manuscript received: July 20, 2024
Revised manuscript received: October 23, 2024
Accepted manuscript online: October 31, 2024
Version of record online: ■■, ■■

RESEARCH ARTICLE

Ceria's oxygen storage and Ce^{3+}/Ce^{4+} switching make it essential in catalysis. In situ tracking of these states is key to understanding reactions. We explore X-ray Raman Scattering (XRS) to observe bulk oxidation states under realistic conditions, comparing results with in situ X-ray Diffraction (XRD).

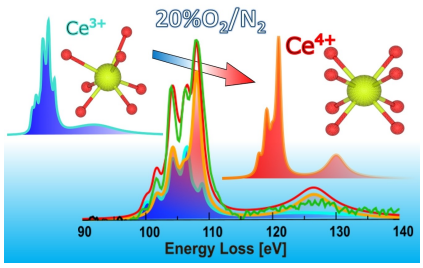

S. K. Das, A. Longo, E. Bianchi, C. V. Bordenca, C. J. Sahle, M. Pia Casaletto, A. Mirone*, F. Giannici*